UROGENITAL IMAGING

I J Radiol. 2026 March; 23(1): e170671 https://doi.org/10.5812/iranjradiol-170671

Published Online: 2026 March 31

Research Article

# Quantitative Assessment of Bone Lesions in Prostate Cancer: Diagnostic Performance of CT Hounsfield Units in Differentiating Metastases From Benign Enostoses

Tze Hui Soo [1,*], Siti Nur Atiqah Mohd Jamil [1], Subapriya Suppiah [1]

[1] Faculty of Medicine and Health Sciences, Universiti Putra Malaysia, Serdang, Malaysia

[*] ***Corresponding Author:*** Faculty of Medicine and Health Sciences, Universiti Putra Malaysia, Serdang, Malaysia. Email: suzyhui88@upm.edu.my

**Received:** 20 January, 2026; **Revised:** 19 February, 2026; **Accepted:** 28 March, 2026

## Abstract

**Background:** Prostate carcinoma is the third most common malignancy among Malaysian men, and the skeleton is the most frequent metastatic site. Differentiating benign enostoses from osteoblastic metastases on computed tomography (CT) remains challenging. Although 99mTc-MDP bone scintigraphy is the gold standard, capacity constraints often delay treatment.

**Objectives:** To evaluate the diagnostic performance of CT Hounsfield Unit (HU) measurements in differentiating these lesions and their correlation with systemic biological markers.

**Patients and Methods:** We retrospectively evaluated 1041 sclerotic lesions (860 metastases and 181 benign enostoses) from 105 patients with prostate carcinoma. Mean HU values were recorded. Diagnostic metrics were computed at the lesion level, with adjustment for within-patient clustering using Generalized Estimating Equations (GEE). Optimal thresholds were determined using Receiver Operating Characteristic (ROC) analysis. Biological correlations with Gleason scores and Prostate-Specific Antigen (PSA) levels were analyzed using Spearman correlation and validated with GEE.

**Results:** Mean HU demonstrated exceptional discriminatory power (area under the curve [AUC] = 0.984; 95% confidence interval [CI]: 0.975 - 0.993; $P < 0.001$). The optimal 944.99 HU threshold yielded 90.6% sensitivity, 97.8% specificity, and 99.5% positive predictive value (PPV). After GEE adjustment, histological Gleason grade ($P = 0.098$), systemic PSA ($P = 0.301$), and regional density differences ($P > 0.05$) showed no significant association with lesion density.

**Conclusion:** Quantitative CT attenuation is a highly accurate triage adjunct. In a high-pretest-probability oncological setting, the 944.99 HU threshold confidently rules in benign enostoses, allowing clinicians to safely avoid unnecessary biopsies and optimize nuclear imaging resources.

*Keywords:* Prostate Carcinoma, Sclerotic Bone Metastases, Hounsfield Units, Osteoblastic Response, Diagnostic Accuracy

## 1. Background

The skeleton is the most frequent metastatic site in advanced prostate carcinoma (PCa), occurring in up to 90% of cases. In Malaysia, PCa represents the third most common male malignancy, with a lifetime risk of 1 in 117 (1, 2). Beyond the epidemiological statistics, progression to bony metastases is a debilitating hallmark of the disease, often precipitating skeletal-related events, severe pain, and a marked decline in quality of life. Effective management relies on timely detection. Although international protocols from the European Association of Urology and American Urological Association recommend bone scintigraphy for patients with prostate-specific antigen (PSA) levels > 20 ng/mL or Gleason scores ≥ 7, the reality in low- and middle-income nations is often defined by logistical capacity constraints (3). Resource constraints in the public sector mean that nuclear medicine wait times are often prolonged, creating a critical delay in treatment initiation.

The primary diagnostic challenge on computed tomography (CT) lies in differentiating benign enostoses from osteoblastic metastases. Although both



**How to Cite:** Soo TH, Mohd Jamil SNA, Suppiah S. Quantitative Assessment of Bone Lesions in Prostate Cancer: Diagnostic Performance of CT Hounsfield Units in Differentiating Metastases From Benign Enostoses. I J Radiol. 2026;23(1):e170671. doi: https://doi.org/10.5812/iranjradiol-170671

appear as hyperdense foci, their clinical implications are diametrically opposed. Enostoses consist of mature, compact lamellar bone that mimics the cortex, resulting in consistently high attenuation. Conversely, prostate cancer metastases are the byproduct of a "vicious cycle" of chaotic remodeling (4, 5). Neoplastic infiltration triggers rapid, haphazard woven bone deposition that lacks native dense mineralization. Traditionally, subjective morphological features, such as irregular margins used to identify metastatic bony foci, have yielded inconclusive results and are prone to interobserver variability. Quantitative analysis using Hounsfield Units (HU) provides an objective alternative by exploiting the physiological mineral density differences between these two entities. Previous research has sought to quantify this density gap, with landmark studies suggesting HU thresholds near 885 can diagnose benign enostoses with > 95% specificity (4, 5). However, these thresholds are not static because treatment can densify malignant lesions, effectively narrowing the diagnostic window (6). Accurate characterization is also vital for guiding contemporary interventional therapies, such as CT-guided microwave ablation, which has emerged as an effective option for treating symptomatic bone metastases (7).

## 2. Objectives

This study aimed to evaluate the diagnostic performance of CT HU measurements in differentiating osteoblastic metastases from benign enostoses within a Malaysian PCa cohort and to establish locally validated attenuation thresholds to support clinical workflow and optimize the utilization of nuclear medicine resources.

## 3. Patients and Methods

This retrospective cross-sectional study was conducted at Hospital Sultan Abdul Aziz Shah (HSAAS), Universiti Putra Malaysia (UPM), in accordance with the principles of the Declaration of Helsinki. Ethical approval was granted by the Institutional Research Ethics Committee of UPM (reference number: JKEUPM-2025-1129). Informed consent was waived because of the retrospective nature of the study and the use of de-identified imaging data retrieved from the Picture Archiving and Communication System (PACS). To minimize selection bias, we consecutively sampled eligible PCa patients diagnosed between January 2022 and December 2025 using electronic medical records. Inclusion criteria required histopathologically confirmed PCa and bone status verification using 99mTc-MDP bone scintigraphy. We excluded patients with primary bone tumors, equivocal bone scintigraphy findings, and those who had received prior systemic treatment to ensure that the observed lesion density reflected the native osteoblastic response rather than treatment-induced sclerosis (Figure 1). Only complete datasets were evaluated, and no data imputation was performed for excluded cases. The sample size was determined using the area under the ROC curve (AUC) as the primary endpoint. A minimum of 95 cases comprising an equal ratio of metastases and benign enostoses was required to achieve 80% power and a statistically significant difference between the AUC of CT HU. The final cohort of 105 patients yielding 1041 lesions (860 metastases and 181 benign enostoses) substantially exceeded the initial requirement and ensured high precision for both threshold validation and anatomical subgroup analyses.

Digital Imaging and Communications in Medicine (DICOM) images from both CT and bone scintigraphy (99mTc-MDP) were retrieved from the PACS system of HSAAS, UPM. CT images were acquired using a 128-slice Siemens SOMATOM scanner (tube voltage, 120 kVp; standard bone reconstruction kernel) with contrast-enhanced imaging. Because densely mineralized osteoblastic lesions are predominantly avascular, intravenous contrast has a negligible effect on their attenuation, ensuring reliable HU quantification. Because of the retrospective design, the reference standard (99mTc-MDP scintigraphy) was interpreted historically during routine care by nuclear medicine physicians. They had access to staging CTs for anatomical correlation but were unaware of this study and its quantitative HU measurements. The radiologist with 5 years of oncological experience who performed HU measurements was blinded to clinical data (e.g., PSA and Gleason score) but used historical scintigraphy reports solely to localize confirmed lesions for targeted region of interest (ROI) placement. Subjective bias was further mitigated by relying strictly on objective, computer-generated HU values. Metastases were defined by focal intense radiopharmaceutical uptake not attributable to trauma or degenerative disease, and benign enostoses were defined by a lack of tracer uptake. Measurements were assessed on 1-mm axial CT slices. A circular ROI was manually drawn within the densest portion of the sclerotic lesion ≥ 5 mm, strictly maintaining a 1 - 2 mm buffer from the lesion periphery and adjacent normal bone to prevent partial volume averaging (Figure 2). For heterogeneous lesions, the ROI was localized exclusively to the focal area of maximum osteoblastic sclerosis. Measurements were repeated twice per lesion and averaged for final analysis.

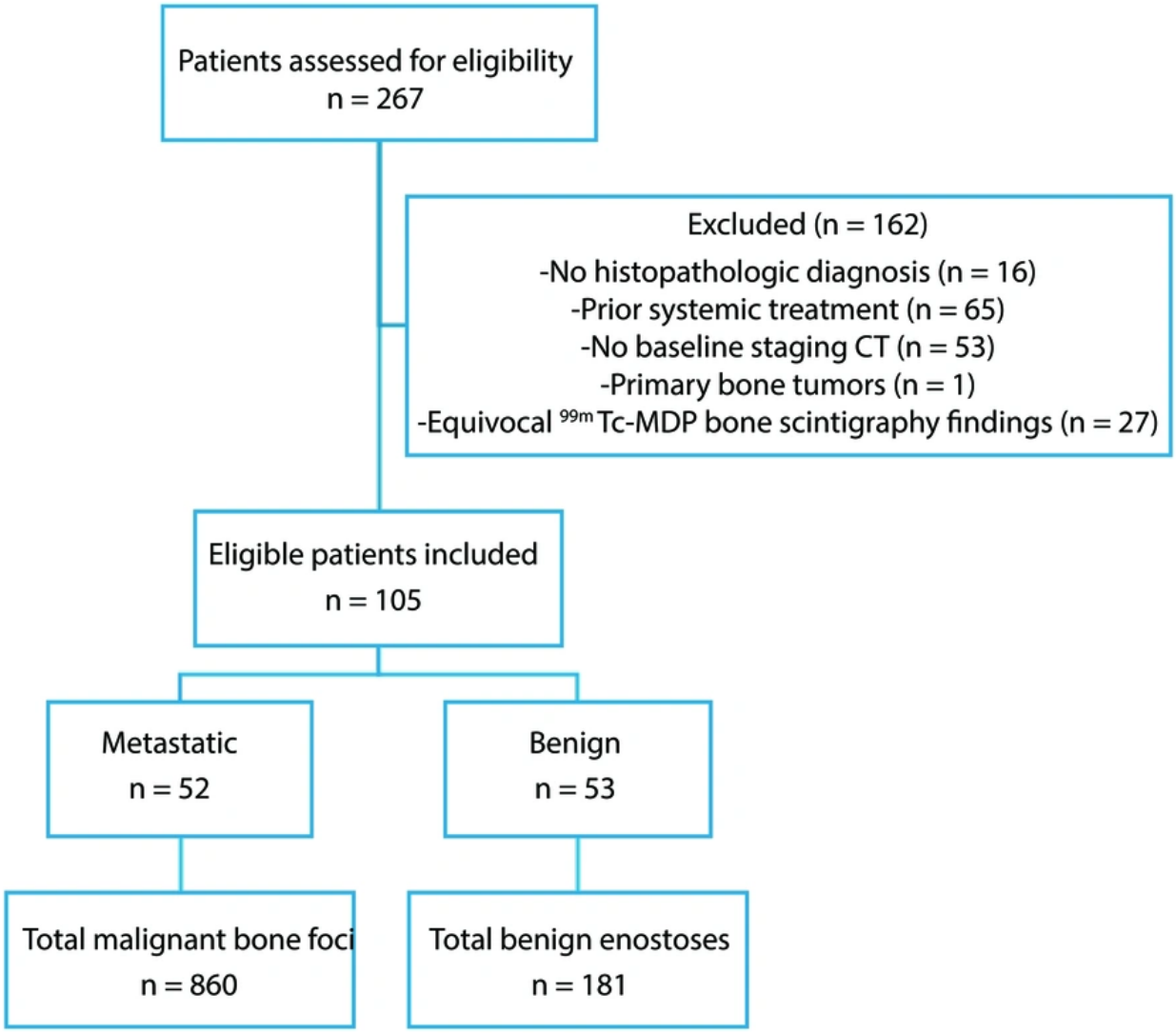


**Figure 1.** STARD flow diagram illustrating the consecutive sampling process, handling of exclusions and indeterminate data, and the final unit of analysis (105 patients yielding 1041 lesions).

Data were analyzed using IBM SPSS Statistics version 29.0 (IBM Corp., Armonk, NY, USA). To account for the potential within-patient clustering effect of multiple lesions nested within an individual patient, Generalized Estimating Equations (GEE) with a binary logistic link and adjusted standard errors were employed. Receiver Operating Characteristic curve analysis and the Youden Index were used to determine the optimal diagnostic threshold, which was an exploratory, data-driven analysis. Internal validation was performed using a random split-sample technique (70% training set and 30% validation set). Precision for all diagnostic estimates was reported using 95% confidence intervals (CIs). Group differences in density based on Gleason scores and anatomical locations were analyzed using the Kruskal-Wallis H test. The influence of biological markers (Gleason score and PSA) was quantified using Spearman correlation and GEE-adjusted regression ($P < 0.05$ was considered statistically significant).

## 4. Results

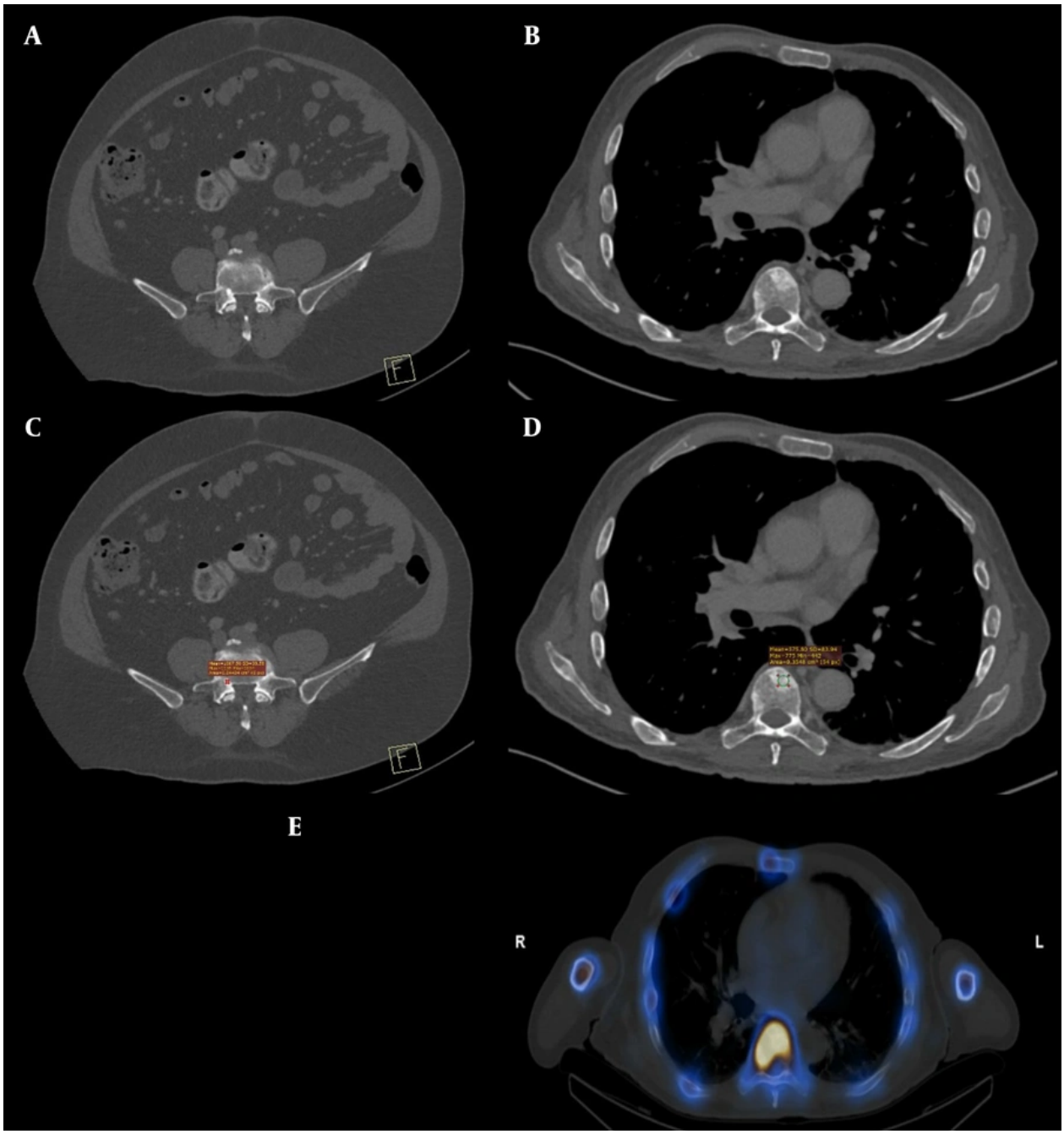


**Figure 2.** Representative CT imaging and region of interest placement with scintigraphy correlation. A and C, Axial contrast-enhanced CT demonstrating a benign enostosis. The circular region of interest is placed strictly at the visual epicenter (maximum sclerosis), maintaining a peripheral buffer to avoid partial volume averaging (mean HU: > 1000); B and D, Axial contrast-enhanced CT demonstrating an osteoblastic metastasis in a thoracic vertebral body with identical epicenter-focused region of interest placement (mean HU: ~575); E, Corresponding 99mTc-MDP bone scintigraphy for the metastatic lesion demonstrates intense focal radiotracer uptake confirming malignancy.

### *4.1. Patient-Level Demographics*

The 105 patients were evenly distributed between the benign enostosis (n = 53) and metastatic groups (n = 52).

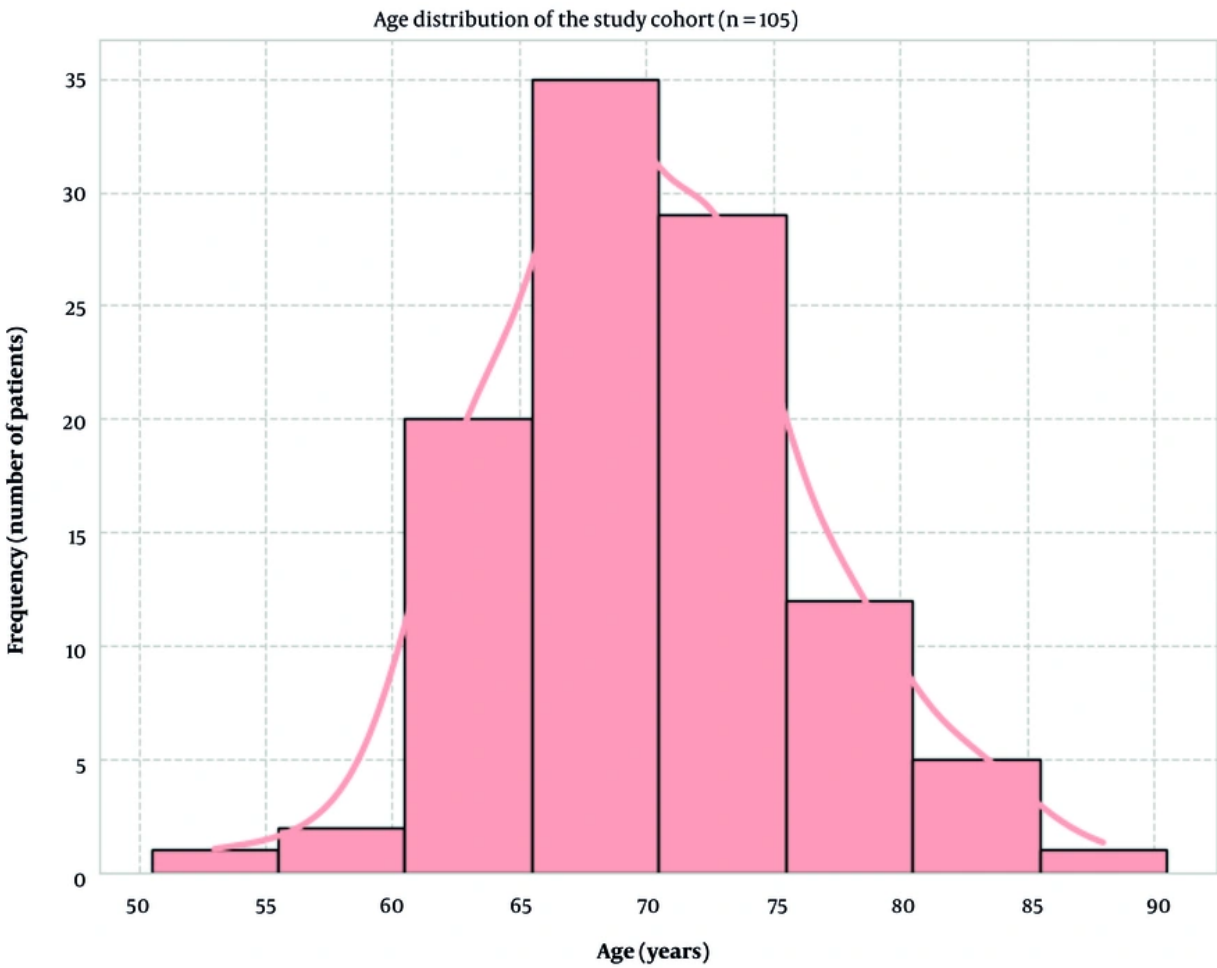


**Figure 3.** Age profile of the study cohort. Histogram showing the age distribution (in years) of the total patient population (n = 105). The cohort mean age was 70.0 ± 6.0 years, consistent with typical prostate carcinoma clinical presentations.

The mean age of the patients was 70.0 ± 6.0 years (range, 52 - 86 years) (Figure 3), aligning with the expected clinical demographic for advanced prostate carcinoma. Baseline biochemical assessment revealed a wide spectrum of disease activity, with a median serum PSA level of 28.0 ng/mL (minimum, 2.9 ng/mL; maximum, 3496.0 ng/mL). Histological analysis of the metastatic group (Figure 4) showed a high prevalence of aggressive disease, with Gleason score 9 being the most frequent grade, identified in 44.2% (n = 23). This was followed by Gleason score 8 (23.1%, n = 12) and Gleason score 7 (17.3%, n = 9).

### 4.2. Lesion-Level Characteristics and Distribution

Across the 105 patients, a total of 1041 sclerotic bony lesions were identified and quantitatively analyzed. Of these, 860 (82.6%) were malignant metastases, while 181 (17.4%) were benign enostoses. The metastatic foci (n = 860) (Figure 5) demonstrated a marked predilection for the axial skeleton, reinforcing the classical understanding of secondary dissemination in prostate cancer. The pelvis was the most frequent site of deposition, containing 34.8% (n = 299), followed by the spine at 33.3% (n = 286). The ribs and sternum accounted for 23.0% (n = 198), while the appendicular skeleton and skull represented 8.8% and 0.1%, respectively. This

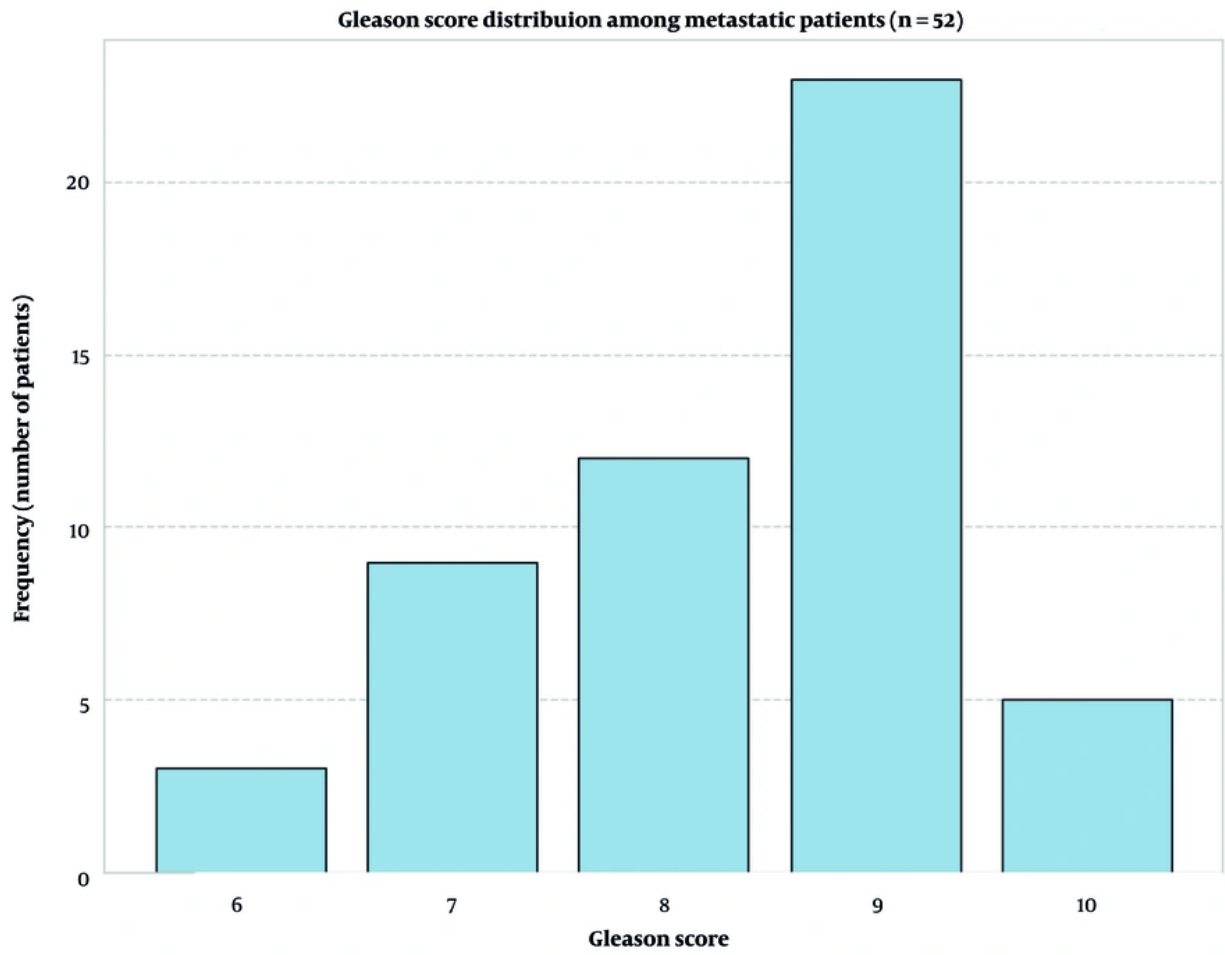


**Figure 4.** Histological grading of metastatic patients. Bar chart showing the distribution of histological Gleason scores among the metastatic patient cohort (n = 52). High-grade disease was present in most patients, with Gleason score 9 being the most prevalent.

distribution is consistent with hematogenous spread via the Batson venous plexus.

### 4.3. Diagnostic Performance of CT Hounsfield Unit Attenuation

Receiver Operating Characteristic analysis for mean HU yielded an AUC of 0.984 (95% CI: 0.975 - 0.993; $P < 0.001$), indicating exceptional diagnostic accuracy (Figure 6). GEE adjustment confirmed that mean HU remained a highly significant independent factor in differentiating metastases from benign enostoses ($P < 0.001$). This confirms that the statistical significance of the radiological density gap was not driven by specific high-burden patients but represented a stable diagnostic metric across the cohort. The Youden Index identified a threshold of 944.99 HU as the optimal cutoff. At this value, the diagnostic performance (dataset prevalence, 82.6%; 860 metastases and 181 benign enostoses) achieved 90.6% sensitivity, 97.8% specificity, 99.5% positive predictive value, 68.3% negative predictive value, 41.18 positive likelihood ratio, and 0.096 negative likelihood ratio. Internal 70/30 split-sample validation confirmed the robustness of the derived threshold. In the training subset (n = 739), ROC analysis yielded an AUC of 0.983 (95% CI: 0.976 - 0.990; $P < 0.001$), identifying an optimal threshold of 944.11 HU (89.9% sensitivity and 97.0% specificity). Applying this derived threshold to the remaining 30% validation subset (n = 302) achieved 91.8% sensitivity and 100.0% specificity.

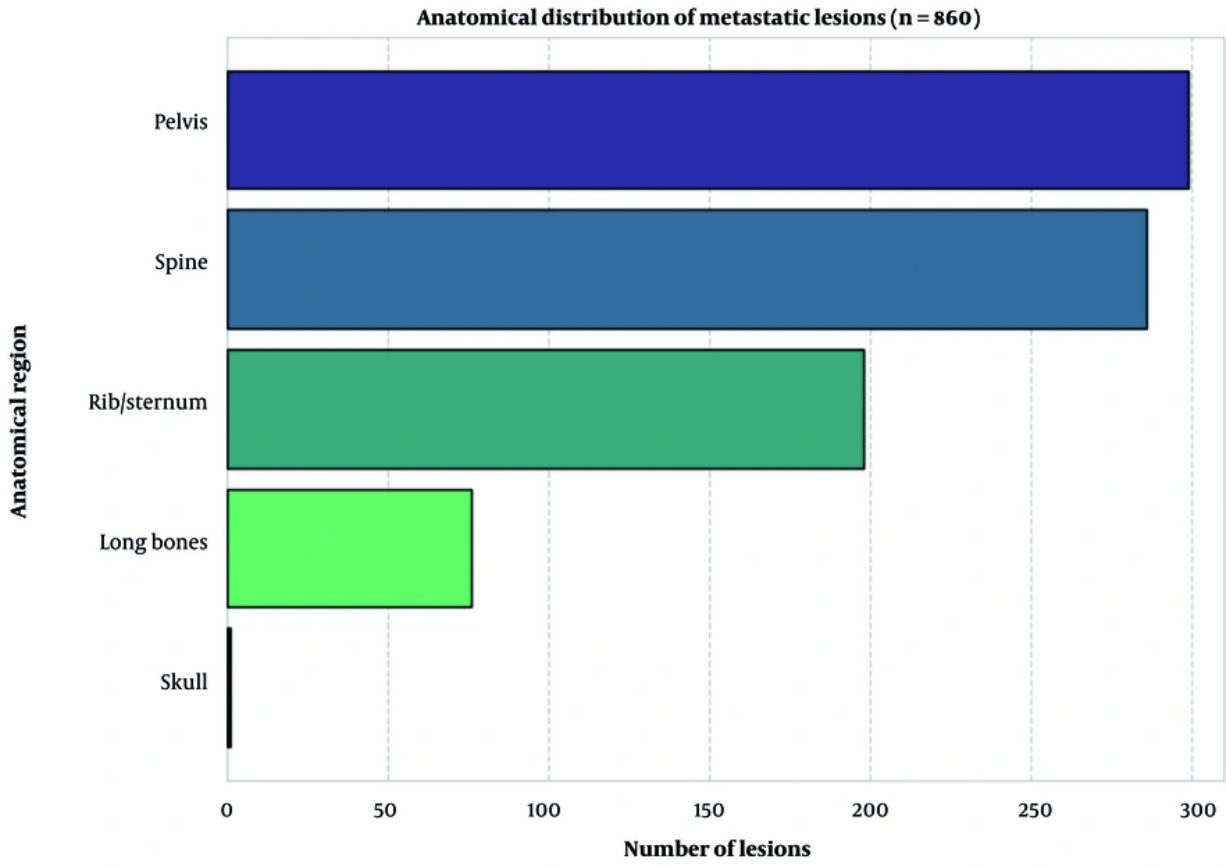


**Figure 5.** Anatomical distribution of metastatic lesions. Frequency distribution of individual metastatic lesions (n = 860) across various skeletal regions. The axial skeleton, particularly the pelvis and spine, represents the most common sites of metastatic involvement.

### *4.4. Influence of Anatomical Location on Mineralization*

Although unadjusted data assessed with the Kruskal-Wallis test suggested significant differences among anatomical sites, GEE analysis revealed no statistically significant differences when using the spine as the reference group (Table 1). Spinal lesions (n = 286) demonstrated a mean density of 680.1 ± 404.8 HU. Spinal lesion density did not significantly differ from densities in the pelvis (mean, 702.5 ± 203.2 HU; P = 0.421), ribs/sternum (mean, 733.5 ± 198.1 HU; P = 0.141), or long bones (mean, 677.7 ± 187.9 HU; P = 0.971).

### *4.5. Correlation Between Biological Markers and Lesion Density*

The relationship between systemic biological indicators and metastatic foci mineralization was assessed using Spearman rank-order correlation and multiple linear regression and was validated through the GEE model. Although unadjusted data suggested a positive association, the GEE model revealed that histological Gleason grade was not independently associated with lesion density (P = 0.098) (Figure 7). Similarly, systemic PSA levels exhibited no significant correlation with the density of individual metastatic lesions (P = 0.301) (Figure 8). These findings indicate a biological dissociation between total systemic tumor burden or primary tumor grade and the localized mineralization process at the specific metastatic site.

## 5. Discussion

### *5.1. Establishing a Diagnostic Threshold for Clinical Safety*

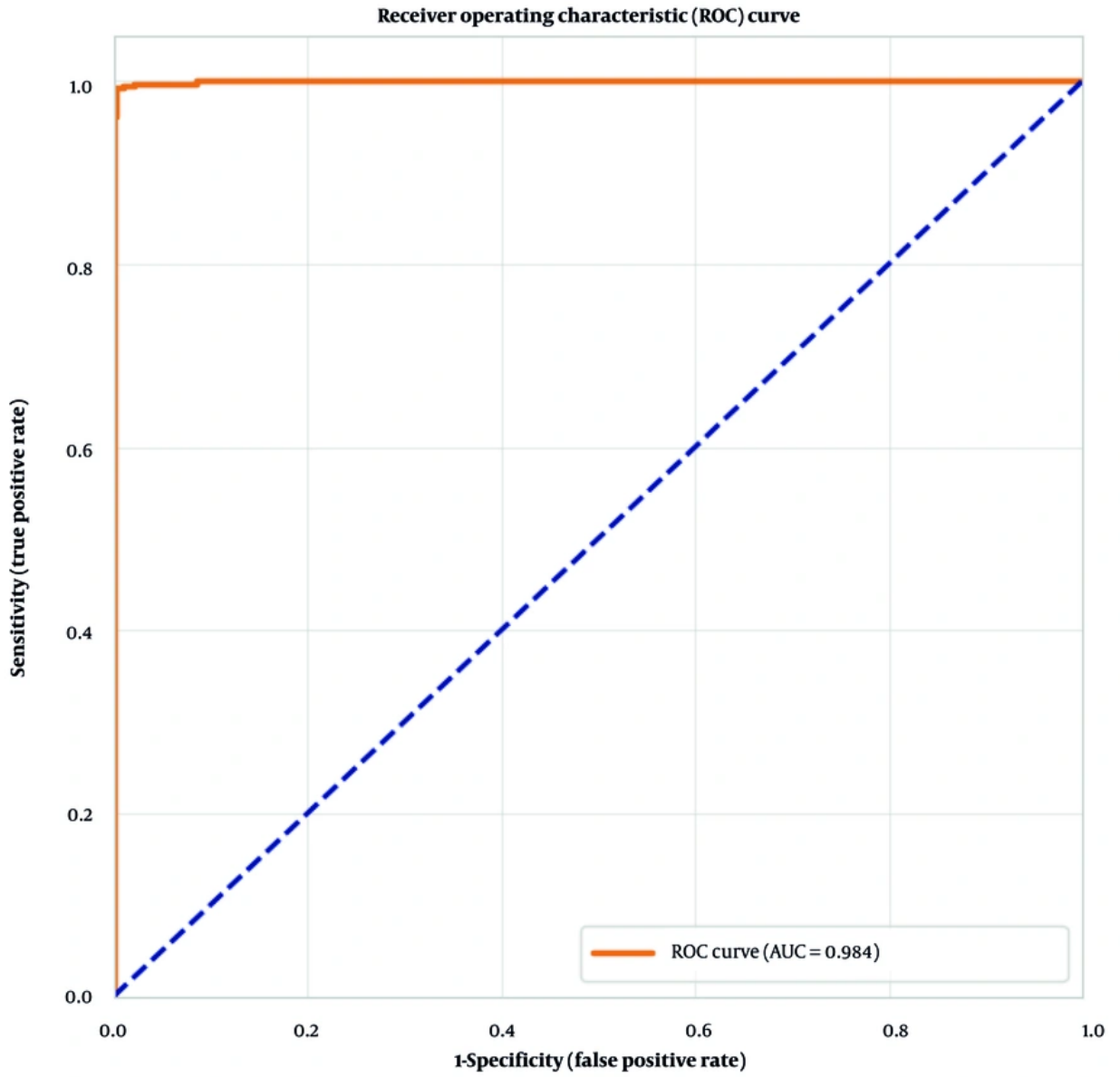


**Figure 6.** Receiver Operating Characteristic curve analysis for the performance of mean CT attenuation. Receiver Operating Characteristic curve evaluating the diagnostic performance of mean computed tomography attenuation, measured in Hounsfield Units. The area under the curve of 0.984 (95% confidence interval: 0.975 - 0.993) confirms that quantitative Hounsfield Unit measurement is a highly reliable tool for distinguishing malignant sclerotic metastases from benign enostoses.

Quantitative CT attenuation is a distinctly modern diagnostic pursuit that gained traction only with the widespread adoption of advanced multidetector CT scanners in the last decade. A comprehensive review of the literature revealed no seminal studies evaluating this specific quantitative thresholding technique before 2010. Although contemporary research frequently cites an 885 HU diagnostic benchmark (4), these foundational studies often relied on highly heterogeneous cohorts (breast, lung, prostate malignancies, etc.) and pooled data across varying CT scanner models (4-6, 8-10). Such biological and hardware-related variables inherently introduce wide HU fluctuations, leading some recent studies to report conflicting accuracies. Our study

**Table 1.** Regional Heterogeneity of Metastatic Mineralization [a]

| Variables | Lesions (n) | Mean HU (± SD) | P-Value |
|---|---|---|---|
| **Spine** | 286 | 680.1 ± 404.8 | — |
| **Pelvis** | 299 | 702.5 ± 203.2 | 0.421 |
| **Rib/Sternum** | 198 | 733.5 ± 198.1 | 0.141 |
| **Long Bones** | 76 | 677.7 ± 187.9 | 0.971 |
| **Skull** | 1 | 910.9 | N/A |

Abbreviations: CT, computed tomography; GEE, Generalized Estimating Equations; HU, Hounsfield Units; N/A, not available; SD, standard deviation.

[a] Mean CT attenuation, measured in HU, and SD are categorized by anatomical location for all confirmed metastatic lesions (n = 860). Comparative analysis was performed using GEE with the axial skeleton (spine) as the reference group to account for within-patient clustering.

mitigated these confounders by exclusively evaluating a uniform PCa cohort validated against 99mTc-MDP bone scintigraphy as the reference standard. By eliminating the biological noise of multi-tumor cohorts, the derived 944.99 HU threshold (positive predictive value, 99.5%) provides a highly reliable, disease-specific metric reflecting the vigorous osteoblastic microenvironment unique to advanced PCa. Lesions exceeding 945 HU are highly likely to be benign enostoses, allowing safe de-escalation of diagnostic workups. This robust diagnostic performance is largely consistent with the foundational work conducted at Massachusetts General Hospital (4), which established an 885 HU threshold to distinguish untreated osteoblastic metastases from benign enostoses with a reported sensitivity of 95%. Although foundational studies (4, 5) used the "largest possible ROI" extending to lesion margins, this risks partial volume averaging with adjacent, less dense trabecular bone. Our epicenter-focused approach with a strict 1 - 2 mm buffer ensures that the extracted HU reflects pure lesional matrix, improving specificity. Although our derived threshold is slightly higher than previously reported benchmarks, this likely reflects the distinct histological profile in our Malaysian cohort. As noted in our results, nearly 44% of our patients presented with a Gleason score of 9, suggesting that more aggressive primary phenotypes may stimulate a more vigorous and dense osteoblastic response in the bone microenvironment. As Sala et al. (5) previously observed, quantitative attenuation acts as a powerful discriminatory lever in characterizing sclerotic foci, particularly within treatment-naive populations. By adopting this locally derived threshold, radiologists can increase diagnostic confidence in differentiating sclerotic foci detected on staging CT. Consequently, clinicians can spare patients from unnecessary biopsies and reduce the urgency for nuclear imaging. Conversely, lesions below this threshold remain suspicious, prioritizing these patients for expedited bone scintigraphy.

### 5.2. Site-Specific Mineralization: The Spine vs. Appendicular Skeleton

Unadjusted data suggested that spinal lesions (mean, 680.1 HU) were radiologically less dense than pelvic (702.5 HU) and rib/sternum lesions (733.5 HU). From a physiological perspective, this gradient aligns with the principles described by Kivell (11), which suggest that trabecular bone in the spine exhibits a higher metabolic flux than the more cortical-dense ribs. The hypervascularity and constant remodeling of the spine may dilute the sclerotic response, leading to lower HU values compared with those of more stagnant skeletal sites. Clinically, this implies that a softer lesion in the spine may carry the same malignant weight as a significantly denser lesion in the appendicular skeleton. However, GEE analysis confirmed that these regional density variations did not reach statistical significance. Clinically, this is a highly advantageous finding. It demonstrates that despite inherent baseline differences in regional bone turnover, the profound osteoblastic response driven by metastatic prostate cancer remains remarkably consistent across different skeletal sites within the same patient. Consequently, our derived diagnostic threshold of 945 HU is remarkably stable; a "softer" lesion in the spine and a denser lesion in the ribs can both be reliably evaluated using this single universal threshold without the need for region-specific calibrations.

### 5.3. The Biological Complexity of the Gleason-Density Relationship

Histological Gleason grade was not significantly associated with localized lesion density (P = 0.098). This indicates that although aggressive, high-grade prostate cancer cells are responsible for initiating the metastatic cascade, the ultimate degree of mineralization is not strictly proportional to the primary tumor histological grade. This aligns with the "Gleason-density paradox"

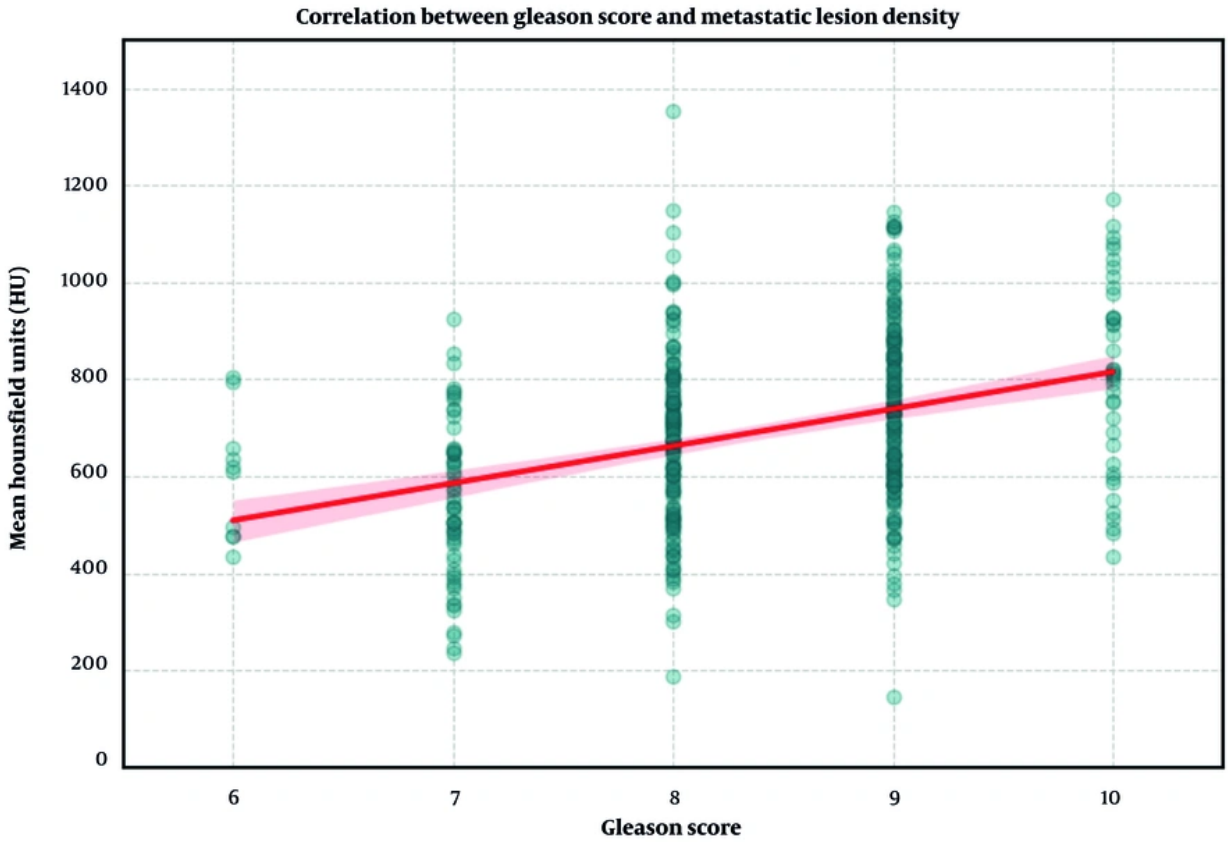


**Figure 7.** Relationship between Gleason score and metastatic lesion density. Scatter plot illustrating the relationship between primary tumor Gleason score and the mean Hounsfield Units of individual metastatic lesions (n = 860). Although the unadjusted raw data display a visual upward trend, Generalized Estimating Equations adjusting for within-patient clustering revealed that this relationship was not statistically significant (P = 0.098).

mechanisms described by Wang et al. (12). Although biological signaling from the prostate initiates the process, the final radiological appearance is largely dictated by the "vicious cycle" of the local bone microenvironment. Local cytokines and host-specific factors appear to have a more profound influence on final mineral density than the original primary tumor grade itself (13).

### 5.4. Prostate-Specific Antigen-Density Dissociation and Resource Management

The lack of correlation between PSA levels and mean HU in our cluster-adjusted GEE model (P = 0.301) differs from common clinical expectations (14) but supports recent findings by Wong et al. (15). Their research suggests that although PSA is an excellent marker of total systemic tumor volume, it does not correlate with the localized degree of osteoblastic response. This underscores the limitation of using systemic markers to predict the radiological characteristics of specific bone lesions. In resource-constrained environments, using mean HU as an adjunct can prioritize the use of nuclear imaging for highly suspicious cases, streamlining the diagnostic workflow without compromising patient safety.

### 5.5. Limitations

This retrospective, single-center study used a single reader, precluding formal interobserver reproducibility metrics, as this fell outside the primary scope of the current study. Future prospective, multicenter, and multireader studies are essential to externally validate these diagnostic metrics, formalize interrater reliability,

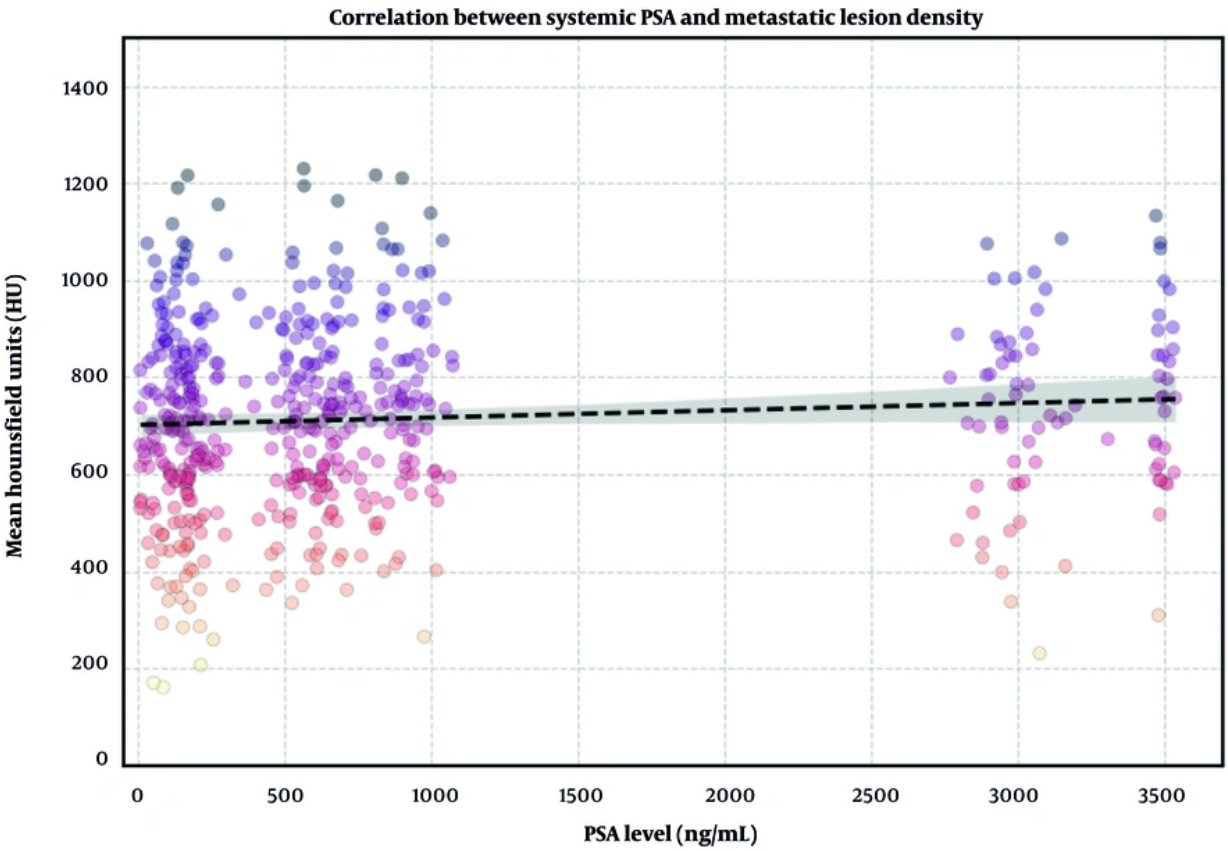


**Figure 8.** Biological dissociation between systemic prostate-specific antigen and metastatic lesion density. Scatter plot illustrating the lack of correlation between systemic prostate-specific antigen levels (measured in ng/mL) and the mean Hounsfield Units of individual metastatic foci (n = 860). Generalized Estimating Equations analysis adjusting for within-patient clustering confirmed no significant correlation (P = 0.301).

and investigate the evolution of HU values during systemic therapy.

In conclusion, quantitative CT HU is a highly accurate objective triage adjunct to bone scintigraphy for differentiating sclerotic lesions in PCa patients undergoing CT staging. The 945 HU threshold provides a robust rule-in tool for benign enostoses (positive predictive value, 99.5%). The lack of significant correlation between systemic markers (Gleason score and PSA) and lesion density reinforces that the final radiological appearance is driven by the local bone microenvironment rather than overall systemic tumor burden. Integrating this threshold into high-pretest-probability contexts enables the safe de-escalation of diagnostic workups, avoids unnecessary biopsies, and prioritizes urgent nuclear imaging for true metastatic suspects.

## Footnotes

**AI Use Disclosure:** The authors declare that no generative AI tools were used in the creation of this article.

**Authors' Contribution:** Study concept and design: T. H. S., S. N. A. M. J., and S. P.; acquisition of data, analysis, and interpretation of data: T. H. S. and S. N. A. M. J.; drafting of the manuscript: T. H. S. and S. N. A. M. J.; critical revision of the manuscript for important intellectual content: T. H. S. and S. P.; statistical analysis: T. H. S. and S. N. A. M. J.; administrative, technical, and material support: T. H. S. and S. P.; and study supervision: T. H. S. and S. P.

**Conflict of Interests Statement:** The authors do not declare any conflicts of interests for this study.

**Data Availability:** The dataset presented in this study is available on request from the corresponding author during submission or after publication. The data are not publicly available due to privacy and ethical restrictions, as they contain sensitive clinical information from prostate cancer patients that could compromise participant confidentiality.

**Ethical Approval:** This study was conducted in accordance with the principles of the Declaration of Helsinki. Ethical approval was granted by the Institutional Research Ethics Committee of Universiti Putra Malaysia (reference number: JKEUPM-2025-1129).

**Funding/Support:** This research was funded by Universiti Putra Malaysia through GP-IPM/2023/9771200.

## References

1. Malaysian National Cancer Registry. Malaysian National Cancer Registry Report 2017 - 2021. *Malaysian National Cancer Registry Report*. 2024.
2. Lim J, Malek R, Jr S, Toh CC, Sundram M, Woo SYY, et al. Prostate cancer in multi-ethnic Asian men: Real-world experience in the Malaysia Prostate Cancer (M-CaP) Study. *Cancer Med*. 2021;**10**(22):8020-8028. [PubMed ID: 34626088]. [PubMed Central ID: PMC8607241]. https://doi.org/10.1002/cam4.4319.
3. Mottet Nicolas, van den Bergh RoderickCN, Briers Erik, Van den Broeck Thomas, Cumberbatch MarcusG, De Santis Maria, et al. EAU-EANM-ESTRO-ESUR-SIOG Guidelines on Prostate Cancer - 2020 Update. Part 1: Screening, Diagnosis, and Local Treatment with Curative Intent. *Eur Urol*. 2021;**79**(2):243-262. [PubMed ID: 33172724]. https://doi.org/10.1016/j.eururo.2020.09.042.
4. Ulano A, Bredella MA, Burke P, Chebib I, Simeone FJ, Huang AJ, et al. Distinguishing Untreated Osteoblastic Metastases From Enostoses Using CT Attenuation Measurements. *AJR Am J Roentgenol*. 2016;**207**(2):362-368. [PubMed ID: 27101076]. https://doi.org/10.2214/AJR.15.15559.
5. Sala F, Dapoto A, Morzenti C, Firetto MC, Valle C, Tomasoni A, et al. Bone Islands Incidentally Detected on Computed Tomography: Frequency of Enostosis and Differentiation From Untreated Osteoblastic Metastases Based on CT Attenuation Value. *Br J Radiol*. 2019;**92**(1103):20190249. [PubMed ID: 31469323]. [PubMed Central ID: PMC6849660]. https://doi.org/10.1259/bjr.20190249.
6. Elangovan SM, Sebro R. Accuracy of CT Attenuation Measurement for Differentiating Treated Osteoblastic Metastases From Enostoses. *AJR Am J Roentgenol*. 2018;**210**(3):615-620. [PubMed ID: 29323547]. https://doi.org/10.2214/AJR.17.18638.
7. Hao B, Ma J, Wan N, Xu S, Wang Z. Therapeutic Effects of CT-Guided Microwave Ablation Combined with Cementoplasty in the Treatment of Bone Metastasis. *I J Radiol*. 2023;**20**(3):e128065. https://doi.org/10.5812/ijradiol-128065.
8. Kosinipalli Naveen kumar, Patnaik Sujata, S Rammurti. Role of CT Attenuation Value in Differentiating Enostosis From Osteoblastic Metastases. *Global Journal for Research Analysis*. 2020;**9**(10).
9. Priyanka K, Deep ChaitanyaDSJ, Babu OSridhar. Utility of CT Attenuation Value in Differentiating Enostosis From Untreated Osteoblastic Metastases. *Int J Med Pub Health*. 2025;**15**(4):170-174.
10. Lee HarrisonT, Pryma DanielA, Sebro Ronnie. Optimized CT Attenuation and SUV Prediction Thresholds for Differentiating Enostoses From Untreated and Treated Metastases on Attenuation-Corrected 18F-FDG PET/CT. *Clin Nucl Med*. 2020;**45**(1):32-37. [PubMed ID: 31693615]. https://doi.org/10.1097/RLU.0000000000002808.
11. Kivell TL. A Review of Trabecular Bone Functional Adaptation: What Have We Learned From Trabecular Analyses in Extant Hominoids and What Can We Apply to Fossils? *J Anat*. 2016;**228**(4):569-594. [PubMed ID: 26879841]. [PubMed Central ID: PMC4804137]. https://doi.org/10.1111/joa.12446.
12. Wang H, Zhang W, Bado I, Zhang XH. Bone Tropism in Cancer Metastases. *Cold Spring Harb Perspect Med*. 2019;**10**(10):a036848. [PubMed ID: 31615871]. [PubMed Central ID: PMC7528862]. https://doi.org/10.1101/cshperspect.a036848.
13. Huang G, Hou T, Song D, Meng T. The Regulatory Networks and Mechanisms of Bone Microenvironment in Tumorigenesis and Metastasis. *J Bone Oncol*. 2025;**55**:100729. [PubMed ID: 41399767]. [PubMed Central ID: PMC12702220]. https://doi.org/10.1016/j.jbo.2025.100729.
14. Zhang X, Jiang P, Wang C. The Role of Prostate-Specific Antigen in the Osteoblastic Bone Metastasis of Prostate Cancer: A Literature Review. *Front Oncol*. 2023;**13**:1127637. [PubMed ID: 37746292]. [PubMed Central ID: PMC10513387]. https://doi.org/10.3389/fonc.2023.1127637.
15. Wong SK, Mohamad NV, Giaze TR, et al. Prostate Cancer and Bone Metastases: The Underlying Mechanisms. *Int J Mol Sci*. 2019;**20**(10):2587. [PubMed ID: 31137764]. [PubMed Central ID: PMC6567184]. https://doi.org/10.3390/ijms20102587.